Distinction of Electron Dispersion in Time-Resolved Photoemission Spectroscopy

Qing Liao,[1,*] Wei Cao,[2] Qingbin Zhang,[2] Kai Liu,[1] Feng Wang,[1] Peixiang Lu,[1,2,3,†] and Uwe Thumm[4,‡]

[1]Hubei Key Laboratory of Optical Information and Pattern Recognition, Wuhan Institute of Technology, Wuhan 430205, China
[2]Wuhan National Laboratory for Optoelectronics and School of Physics, Huazhong University of Science and Technology, Wuhan 430074, China
[3]CAS Center for Excellence in Ultra-intense Laser Science, Shanghai 201800, China
[4]Department of Physics, Kansas State University, Manhattan, Kansas 66506, USA

While recent experiments provided compelling evidence for an intricate dependence of attosecond photoemission-time delays on the solid's electronic band structure, the extent to which electronic transport and dispersion in solids can be imaged in time-resolved photoelectron (PE) spectra remains poorly understood. Emphasizing the distinction between photoemission time delays measured with two-photon, two-color interferometric spectroscopy, and transport times, we demonstrate how the effect of energy dispersion in the solid on photoemission delays can, in principle, be observed in interferometric photoemission. We reveal analytically a scaling relation between the PE transport time in the solid and the observable photoemission delay and confirm this relation in numerical simulations for a model system. We trace photoemission delays to the phase difference the PE accumulates inside the solid and, in particular, predict negative photoemission delays. Based on these findings, we suggest a novel time-domain interferometric solid-state energy-momentum-dispersion imaging method.

Attosecond spectroscopic techniques have been extensively employed to investigate time-resolved photoelectron (PE) emission from gaseous atomic [1–4] and solid targets [5–12] for more than a decade. For solid targets, photoemission time delays are usually interpreted as the transport time for ballistic electron transport in the solid [5–8,10,12]. This ballistic transport mechanism is challenged by a recent reconstruction of attosecond beats by interference of two-photon transitions (RABITT) experiment with solid targets by Locher et al. [8]. Their experiment reveals an intricate dependence of photoemission delays (phases) on the final PE kinetic energy ε_f for photoemission from the 4d band of Ag(111) and 5d band of Au(111) surfaces, drastically deviating from the predictions of a classical free-electron transport model. Surprisingly, the measured time delays for Ag(111) alternate rapidly between large *negative* and large *positive* values as a function of ε_f, blatantly contradicting the ballistic mechanism. Similar pronounced phase changes in RABITT spectra were observed from Ni(111) and Cu (111) surfaces [9,13] and understood as final-state shape resonances [14]. RABITT phases measured from the Cu (111) 3d band show a resonancelike increase [10], which the authors interpret as due to non-free-electron propagation and the formation of an effective PE mass across less than two atomic layers [14].

The influence of the PE group velocity derived from band-structure calculations [5,15,16] on the PE transport time can be understood intuitively within transport models [5,8,15,17–20]. However, attosecond spectroscopy

measures the spectrally resolved phase accumulated during the entire photoemission process, i.e., the (spectrally resolved) *phase* velocity of the PE wave packet. It is thus directly related to the PE phase and phase velocities, rather than to the PE *group* velocity. Both the PE group and phase velocity are determined by the solid band structure. Their clear distinction is essential for the insightful tracking of electronic transport and dispersion in time-resolved photoemission spectra, but has not been addressed in time-resolved PE models [5,8,10,15,17–25], to the best of our knowledge.

Separating electronic excitation and propagation in the solid, we here unambiguously demonstrate how electronic dispersion affects the interferometric photoemission-time delay in two-color, two-photon attosecond interferometric photoemission. We take the simplest, i.e., parabolic, dispersion relation as an example. Representing electronic dispersion in the solid by the energy-dependent effective electron mass, we analytically reveal for a simplified model system the scaling law

$$t_{pe,2q} = t_{0,2q} + \alpha(R_{2q})t_{tr,2q+1}, \qquad (1)$$

between the PE transport time in the solid $t_{tr,2q+1}$ and the photoemission-time delay $t_{pe,2q}$ that is observable in RABITT sideband (SB) spectra. $t_{0,2q}$ is a sample-independent offset. The scaling factor α very sensitively depends on the ratio $R_{2q} = m_{e,2q-1}/m_{e,2q+1}$ between the effective energy-dependent PE masses inside the solid, $m_{e,2q-1}$
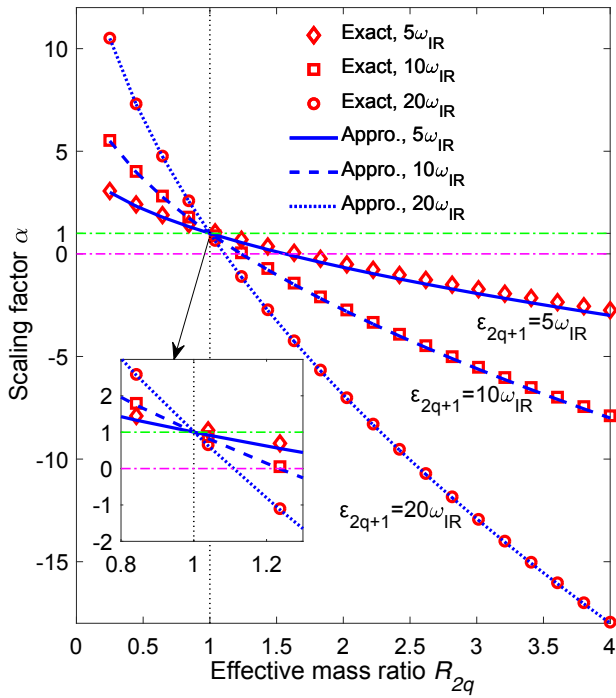
FIG. 1. Scaling factor $\alpha(R_{2q})$ in Eq. (1) as a function of the effective mass ratio R_{2q} of PEs released by successive odd HHs of order $2q \pm 1$ of the XUV APT. Approximate results according to Eq. (5) and exact results for final PE energies $\varepsilon_{2q+1} = 5\omega_{IR}$ (diamonds and solid blue solid line), $10\omega_{IR}$ (squares and dashed blue line), and $20\omega_{IR}$ (circles and dotted blue line). The vertical dotted line indicates equal effective masses with an enlarged view in the inset.

and $m_{e,2q+1}$, for emission by high-harmonic (HH) components of the attosecond pulse trains (APTs) of orders $2q - 1$ and $2q + 1$ with photon energies $(2q - 1)\omega_{IR}$ and $(2q + 1)\omega_{IR}$, respectively (throughout this Letter we use atomic units, unless specified otherwise). The infrared (IR)-laser photon energy is designated as ω_{IR}. A small deviation of R_{2q} from one can significantly change the sign and magnitude of α (Fig. 1). This sensitive dependence of $t_{pe,2q}$ on R_{2q}, and thus on the PE energy, explains the unusual energy dependence of recently measured photoemission-time delays [8]. Below we validate Eq. (1) by numerical solution of the time-dependent Schrödinger equation (TDSE). Based on Eq. (1), we propose a novel method to extract accurately photoemission-time delays for imaging electronic dispersion in real solids, as an important step towards advanced applications of attosecond chronoscopy.

We represent the vector potential of the extreme ultraviolet (XUV) APT with pulse length t_X, in terms of its spectrally narrow odd HH components with amplitudes $A_{X0,2q+1}$ and phases φ_{2q+1}, as $A_X(t) = \sum_q A_{X,2q+1}(t) = f_X(t) \sum_q A_{X0,2q+1} e^{-i[(2q+1)\omega_{IR}t + \varphi_{2q+1}]}$, with the Gaussian temporal envelope $f_X(t) = e^{-2 \ln 2(t/t_X)^2}$. We first focus on the excitation to electronic continuum states in the
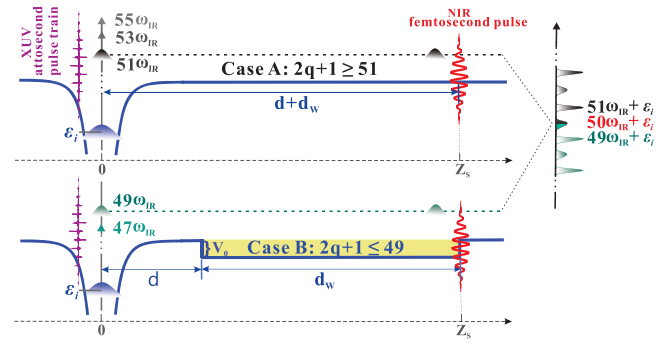

FIG. 2. Model system used to derive the scaling relation in Eqs. (1), (3), and (4). PE dispersion is tunable by adjusting the well depth (barrier height) V_0. Case A depicts free and case B dispersive propagation with effective mass $m_{e,2q+1}$ in a slab of width d_W [Eq. (6)].

solid by the XUV APT at a specific lattice site and generalize our study to XUV photoexcitation in real solids further below. Excited electrons are assumed to traverse a vacuum region of thickness d before propagating across a solid film of thickness d_W (Fig. 2). Upon reaching the solid exit surface, PEs either absorb or emit an IR photon as they move to the detector, forming XUV-IR delay-dependent SB spectra. We represent the IR pulse by the vector potential $A_L(z, t - \tau) = \Theta(z - z_s)A_{L0}(t - \tau) \cos[\omega_{IR}(t - \tau)]$, where Θ is the unit step function. It is delayed by τ relative to the XUV APT and assumed to be fully screened at the exit surface [17] located at $z_s = d + d_W$ (Fig. 2).

At the central SB-$2q$ energy $k_f^2/2 = \varepsilon_i + 2q\omega_{IR}$, the total phase difference between contributions from HH components $2q + 1$ and $2q - 1$, followed by emission and absorption of one IR photon, respectively, is $\Delta\Phi_{2q} = \Delta\xi_{2q}(z) - \Delta\varphi_{2q} - \pi - 2\omega_{IR}\tau$ [26], with $\Delta\varphi_{2q} = \varphi_{2q+1} - \varphi_{2q-1}$ and the relative phase of π between IR photon emission and absorption. The ground-state energy of the model system is denoted as ε_i. Assuming initial states localized at $z = 0$, the spatial propagation-phase difference between the interfering SB channels for the model system becomes

$$\Delta\xi_{2q}(z) = \left(\sqrt{2\varepsilon_{2q+1}} - \sqrt{2\varepsilon_{2q-1}}\right)d + (k_{2q+1} - k_{2q-1})d_W.$$

$$(2)$$

The PE momenta $k_{2q\pm1}$ *inside* the slab correspond to energies $\varepsilon_{2q\pm1} = \varepsilon_i + (2q \pm 1)\omega_{IR}$. Representing the influence of dispersion on the excited electron wave packet in the slab in terms of $m_{e,2q\pm1}$ and writing the group velocity as $v_{g,2q+1} = \sqrt{2\varepsilon_{2q+1}/m_{e,2q+1}}$, the spatial phase accumulation $k_{2q\pm1}d_W = \sqrt{2m_{e,2q\pm1}\varepsilon_{2q\pm1}}d_W$ across the slab width $d_W = v_{g,2q+1}t_{tr,2q+1}$ allows us to identify in Eq. (1) the sample-independent offset

$$t_{0,2q} = \frac{(\sqrt{2\varepsilon_{2q+1}} - \sqrt{2\varepsilon_{2q-1}})d - \Delta\varphi_{2q} - \pi}{2\omega_{IR}} \quad (3)$$

and the scaling factor

$$\alpha(R_{2q}) = \frac{(k_{2q+1} - k_{2q-1})v_{g,2q+1}}{2\omega_{IR}}$$

$$= \frac{\varepsilon_{2q+1}}{\omega_{IR}} - \sqrt{R_{2q}\frac{\varepsilon_{2q+1}}{\omega_{IR}}\left(\frac{\varepsilon_{2q+1}}{\omega_{IR}} - 2\right)}. \quad (4)$$

Equations (1), (3), and (4) quantify the effective mass change between electrons emitted by adjacent odd HH components of the APT on the observable $t_{pe,2q}$. For $\varepsilon_{2q+1} \gg \omega_{IR}$, $\alpha(R_{2q})$ in Eq. (4) becomes

$$\alpha(R_{2q}) \approx \sqrt{R_{2q}} + (1 - \sqrt{R_{2q}})\frac{\varepsilon_{2q+1}}{\omega_{IR}}. \quad (5)$$

It strongly depends on R_{2q} and the energy ratio $\varepsilon_{2q+1}/\omega_{IR}$ (Fig. 1). For $\varepsilon_{2q+1}/\omega_{IR} \geq 5$, Eq. (5) is a very good approximation for Eq. (4).

We validate the scaling relation given by Eqs. (1), (3), and (4) by numerically solving the one-dimensional TDSE for the model depicted in Fig. 2. To pinpoint the effect of energy-dependent PE dispersion on time-resolved photoemission, we emphasize the energy dependence of the PE effective mass,

$$m_{e,2q+1} = \frac{\varepsilon_{2q+1} - V_0}{\varepsilon_{2q+1}}, \quad (6)$$

by representing PE dispersion in the solid in terms of a potential well or barrier with tunable depth $V_0 < 0$ or height $V_0 > 0$, respectively. We consider electron release by a HH component $2q + 1$ of the APT at the specific lattice site with coordinate $z = 0$. The released electron propagates across a well (barrier) of depth (height) V_0 and width d_W with the effective mass (6), starting at position $z = d$. Finally, it is exposed to the IR pulse at the exit surface of the well (barrier) at $z_s = d + d_W$. We set $d = 15$ to avoid distortion of the ground state by $V_0 \neq 0$. We model dispersion in the slab assuming that PEs released by HHs orders $2q + 1 \geq 51$ propagate freely (case A: $V_0 = 0$, i.e., $m_{e,2q+1} = 1$), while electrons excited by HHs of orders $2q + 1 \leq 49$ propagate with an effective mass $m_{e,2q+1} \neq 1$ given in Eq. (6) (case B: $V_0 \neq 0$). We represent the initial photoelectron state ψ_i as the ground state of the Yukawa potential $U_Y(z) = -e^{-|z|/\zeta}/\sqrt{z^2 + a_0^2}$ and adjust the parameters $\zeta = 0.5$ and $a_0 = 0.2735$ to yield $\varepsilon_i = -1$ and negligible Wigner time delays [2].

We assume a continuum-wave IR pulse with a wavelength of 800 nm and an intensity of 10^{11} W/cm². The APT pulse train is simulated using equal peak intensities

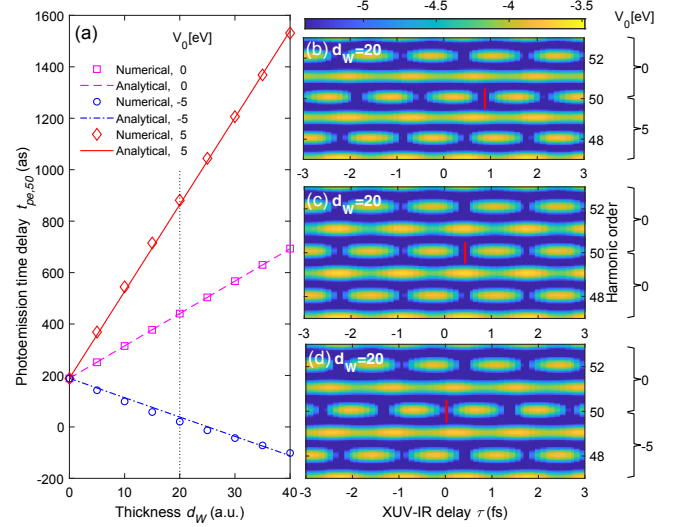

FIG. 3. (a) Simulated photoemission-time delays $t_{pe,50}$ for the model system in Fig. 2 as a function of the transport-region length d_W. The transport region is modeled by a potential well of depth $V_0 = -5$ eV (open circles), free propagation ($V_0 = 0$, open squares), or a barrier of height $V_0 = 5$ eV (open diamonds). Corresponding analytical results from Eqs. (1), (3), and (4) are given by the blue dash-dotted, magenta dashed, and red solid lines. (b)–(d) Quantum-mechanically simulated PE spectra on a logarithmic yield scale versus the APT-IR pulse delay τ for $d_W = 20$ and (b) $V_0 = 5$ eV, (c) 0, and (d) -5 eV. Vertical red lines in (b)–(d) indicate photoemission delay changes relative to $\tau = 0$.

3.5×10^{10} W/cm², phases $\varphi_{2q+1} = 0$, and pulse lengths $t_X = 150$ of its HH constituents. Figures 3(b)–3(d) show coherently added PE spectra from case A and case B in Fig. 2 at different slab thicknesses d_W for $V_0 = -5$, 0, and 5 eV, corresponding to $m_{e,49} = 1.10$, 1.00, and 0.90. The corresponding photoemission-time delays $t_{pe,2q}$ are given in Fig. 3(a) for slab thicknesses between 0 and 40 at SB-50. For each SB, we obtain $t_{pe,2q}$ from the temporal shift of the yield minima relative to $\tau = 0$. The small potential strength $V_0 = \pm 5$ eV entails effective masses that deviate by $\mp$ 10% from the free-electron mass, yet induces remarkably large photoemission delays for SB-50 with respect to other SBs. This is illustrated for $d_W = 20$ by the dotted vertical line in Fig. 3(a) and the vertical red lines in Figs. 3(b)–3(d). This temporal shift remains significant for thicknesses on the length scale of crystal-lattice spacings (a few a.u.) [Fig. 3(a)]. An increase ($m_{e,49} \geq 1$) or decrease ($m_{e,49} \leq 1$) from the free-electron mass results in a negative or positive relative propagation phase $\Delta\xi_{50}(z)$ and scaling factor $\alpha(R_{50})$, respectively. Depending on the HH-phase difference $\Delta\varphi_{50}$ in the offset $t_{0,50}$, according to Eqs. (1), (3), and (4), the delay $t_{pe,50}$ may thus assume both positive and negative values. This may explain the recent observation of negative photoemission delays in RABITT spectra from Al(111) [8]. The quantum mechanically calculated photoemission delays as a function of the slab thickness at

different V_0 in Fig. 3(a) are in excellent agreement with the prediction of our analytical scaling law in Eqs. (1), (3), and (4).

We note that band structure calculations [5,15,16] deviate severely from free-electron dispersion for the considered energies. However, comparing theoretical results with the existing experimental data in a transparent way is difficult within a large-scale, more realistic simulation for mainly two reasons. First, energy-momentum dispersion relations based on density-functional theory (DFT) are not reliable for energies above tens of eV. Second, the spectral range of several eV of the initial valence-band states in the experiment [8] largely averages out the sensitive dispersion dependence of the photoemission time delays. Additional difficulties in real systems arise due to the delocalized nature of valence states, contributions to the photocurrent from different lattice sites, the screening of the IR field at the surface, and the sudden dispersion change at the bulk-vacuum interface. In contrast to RABITT experiments the discussed phase-velocity effects are very difficult, if not impossible, to observe in attosecond streaking experiments, as this would require the deconvolution of spectrally resolved phase information in energetically broad continuous streaking traces.

Advanced applications of attosecond spectroscopy in solids must circumvent these difficulties. Importantly, by choosing strongly localized core-level (CL) states as the initial states, we can avoid the adverse effects of these factors by deducing the photoemission time delay $\delta\tau_{a_s}$ accumulated by PEs traveling over one lattice constant a_s from the total τ-dependent SB yield $I_{SB}(\tau)$. For non-overlapping initial states, the total SB yield is a sum over contributions from N lattice sites,

$$I_{SB}(\tau) = \sum_N I_0 e^{-\frac{(N-1)a_s}{\lambda}} \sin^2\{\omega_{IR}[\tau - \delta\tau_0 - (N-1)\delta\tau_{a_s}]\},$$
$$(7)$$

where I_0 is the maximum photoemission yield from the topmost lattice site ($N = 1$), λ the mean-free path of the electrons at the considered energies, and $\delta\tau_0$ the photoemission time delay of electrons emitted from the topmost lattice site. Fitting the measured total SB yield to the expression $a + b \sin^2[\omega_{IR}(\tau - \tau')]$ [2], the three parameters a, b, τ' determine the values of I_0, $\delta\tau_0$, and $\delta\tau_{a_s}$. Compared to the excitation of initial valence-band states [8,10,30], our scheme has four distinct advantages. First, no reference target for eliminating $\Delta\varphi_{2q}$ and obtaining the absolute photoemission time delay is needed [8,10,30–32]. Second, the effective screening of the IR laser field at the surface, the quantitative description of which on the atomic length is challenging [17,30], becomes irrelevant. Third, complicated dispersion changes at the bulk-vacuum interface are eliminated. The photoemission time delays, induced by IR
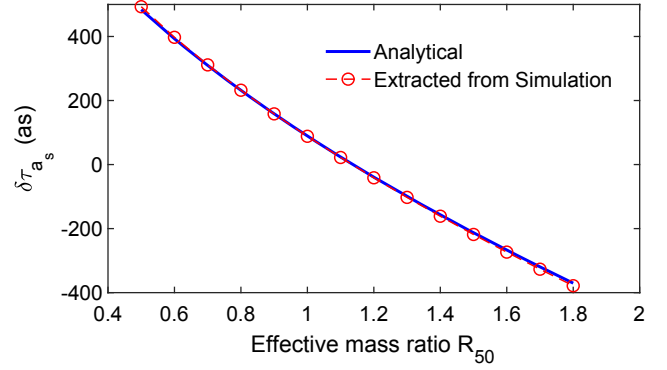

FIG. 4. Photoemission time delays $\delta\tau_{a_s}$ (red circles), for Mg-2p core-level PEs traveling over one lattice constant $a_s = 4.923$ inside solid Mg, extracted from the calculated total τ-dependent SB-50 yield of PEs from 15 lattice sites as a function of the effective mass ratio $R_{50} = m_{e,49}/m_{e,51}$, where $m_{e,51} \equiv 1$. The blue line shows the analytical prediction by Eq. (8).

screening and the change of dispersion at the surface, are collectively included in $\delta\tau_0$. Fourth, core-level states result in much higher PE yields [6], and their narrow SB traces can better be distinguished from HH-emission traces.

According to Eq. (2), the spatial propagation-phase difference over a_s is

$$(k_{2q+1} - k_{2q-1})a_s = 2\omega_{IR}\delta\tau_{a_s}. \qquad (8)$$

Therefore, the measured $\delta\tau_{a_s}$ can be used to obtain the energy-momentum relation $\varepsilon_f(k)$ inside solids by choosing a well-known k_{2q-1} at $\varepsilon_{f,2q-1}$ based on DFT. Next, we show the accuracy of the proposed extraction scheme for simulated τ-dependent SB spectra of Mg-2p CL PEs. We use a semiclassical model to calculate the τ-dependent PE yield at SB-50 [see Eq. (7) in the Supplemental Material [26]]. Mg-2p CL states are modeled by adding a Yukawa potential to the Chulkov potential [24]. The same laser parameters as above and a parabolic dispersion relation in Mg are assumed. We set $\lambda = 10$ a.u. for the considered energies [33]. Figure 4 compares $\delta\tau_{a_s}$ extracted from the calculated total SB-50 yield of PEs emitted from 15 lattice sites and predicted by Eq. (8). We keep $m_{e,51} \equiv 1$ for PEs excited by HH order 51 and change $m_{e,41}$ from 0.5 to 1.8 for PEs excited by HH order 49. As shown in Fig. 4, $\delta\tau_{a_s}$ is deduced accurately according to Eq. (7), suggesting the applicability of Eq. (1) to real solids.

In summary, we related interferometrically measured spectrally resolved PE-emission-time delays t_{pe} to the band structure of the solid target by modeling electronic dispersion in the solid in terms of an energy-dependent PE mass. The photoemission delays are traced to the PE phase difference accumulated inside the solid. We derived analytically and confirmed numerically a strong energy dependence of t_{pe} and revealed the energy- and effective-mass-dependent linear scaling of t_{pe} with the electron-transport time in the

solid. We showed that, even for small deviations from the free-electron mass, the energy dependence of the effective mass can noticeably change t_{pe}. This explains qualitatively the extreme sensitivity of t_{pe} on electron dispersion in recent interferometric photoemission experiments with Au, Ag, Ni, and Cu surfaces [8–10,13]. In particular, we predict negative emission delays t_{pe} [8] while transport times are obviously positive.

Electronic dispersion in solids is usually measured by angle-resolved photoemission spectroscopy [34], where PE momenta along the surface normal are determined based on energy conservation, assuming *free-electron-like* states *inside* the substrate. In contrast, as demonstrated here, attosecond time-resolved interferometric spectroscopy addresses the material-dependent change of PE phase velocities inside the solids, directly providing information on the energy-momentum dispersion. Extracting the time delay t_{pe,a_s} accumulated over one lattice constant from measured SB spectra of CL electrons largely eliminates surface effects. It thus indicates a novel time domain approach to measure PE dispersion and field-driven collective electronic dynamics [35] in solids.

---

[*]liaoqing@wit.edu.cn
[†]lupeixiang@mail.hust.edu.cn
[‡]thumm@phys.ksu.edu

[1] M. Schultze *et al.*, Science **328**, 1658 (2010).
[2] K. Klünder, J. M. Dahlström, M. Gisselbrecht, T. Fordell, M. Swoboda, D. Guénot, P. Johnsson, J. Caillat, J. Mauritsson, A. Maquet, R. Taïeb, and A. L'Huillier, Phys. Rev. Lett. **106**, 143002 (2011).
[3] M. Isinger, R. J. Squibb, D. Busto, S. Zhong, A. Harth, D. Kroon, S. Nandi, C. L. Arnold, M. Miranda, J. M. Dahlström, E. Lindroth, R. Feifel, M. Gisselbrecht, and A. L'Huillier, Science **358**, 893 (2017).
[4] J. Vos, L. Cattaneo, S. Patchkovskii, T. Zimmermann, C. Cirelli, M. Lucchini, A. Kheifets, A. S. Landsman, and U. Keller, Science **360**, 1326 (2018).
[5] A. L. Cavalieri, N. Müller, Th. Uphues, V. S. Yakovlev, A. Baltuška, B. Horvath, B. Schmidt, L. Blümel, R. Holzwarth, S. Hendel, M. Drescher, U. Kleineberg, P. M. Echenique, R. Kienberger, F. Krausz, and U. Heinzmann, Nature (London) **449**, 1029 (2007).
[6] S. Neppl, R. Ernstorfer, E. M. Bothschafter, A. L. Cavalieri, D. Menzel, J. V. Barth, F. Krausz, R. Kienberger, and P. Feulner, Phys. Rev. Lett. **109**, 087401 (2012).
[7] U. Thumm, Q. Liao, E. M. Bothschafter, F. Süßmann, M. F. Kling, and R. Kienberger, in *The Oxford Handbook of Innovation*, edited by D. Andrew (Wiley, New York, 2015), Chap. 13.
[8] R. Locher, L. Castiglioni, M. Lucchini, M. Greif, L. Gallmann, J. Osterwalder, M. Hengsberger, and U. Keller, Optica **2**, 405 (2015).
[9] Z. Tao, C. Chen, T. Szilvási, M. Keller, M. Marikakis, H. Kapteyn, and M. Murnane, Science **353**, 62 (2016).
[10] L. Kasmi, M. Lucchini, L. Castiglioni, P. Kliuiev, J. Osterwalder, M. Hengsberger, L. Gallmann, P. Krüger, and U. Keller, Optica **4**, 1492 (2017).
[11] F. Siek, S. Neb, P. Bartz, M. Hensen, C. Strüber, S. Fiechter, M. Torrent-Sucarrat, V. M. Silkin, E. E. Krasovskii, N. M. Kabachnik, S. Fritzsche, R. D. Muiño, P. M. Echenique, A. K. Kazansky, N. Müller, W. Pfeiffer, and U. Heinzmann, Science **357**, 1274 (2017).
[12] M. Ossiander, J. Riemensberger, S. Neppl, M. Mittermair, M. Schäffer, A. Duensing, M. S. Wagner, R. Heider, M. Wurzer, M. Gerl, M. Schnitzenbaumer, J. V. Barth, F. Libisch, C. Lemell, J. Burgdörfer, P. Feulner, and R. Kienberger, Nature (London) **561**, 374 (2018).
[13] C. Chen, Z. Tao, A. Carra, P. Matyba, T. Szilvási, S. Emmerich, M. Piecuch, M. Keller, D. Zusin, S. Eich, M. Rollinger, W. You, S. Mathias, U. Thumm, M. Mavrikakis, M. Aeschlimann, P. M. Oppeneer, H. Kapteyn, and M. Murnane, Proc. Natl. Acad. Sci. U.S.A. **114**, E5300 (2017).
[14] M. J. Ambrosio and U. Thumm, Phys. Rev. A **100**, 043412 (2019).
[15] E. E. Krasovskii, Phys. Rev. B **84**, 195106 (2011).
[16] E. E. Krasovskii, C. Friedrich, W. Schattke, and P. M. Echenique, Phys. Rev. B **94**, 195434 (2016).
[17] S. Neppl, R. Ernstorfer, A. L. Cavalieri, C. Lemell, G. Wachter, E. Magerl, E. M. Bothschafter, M. Jobst, M. Hofstetter, U. Kleineberg, J. V. Barth, D. Menzel, J. Burgdörfer, P. Feulner, and F. Kra, Nature (London) **517**, 342 (2015).
[18] Q. Liao and U. Thumm, Phys. Rev. A **92**, 031401(R) (2015).
[19] M. J. Ambrosio and U. Thumm, Phys. Rev. A **97**, 043431 (2018).
[20] C. Lemell, B. Solleder, K. Tőkési, and J. Burgdörfer, Phys. Rev. A **79**, 062901 (2009).
[21] Q. Liao and U. Thumm, Phys. Rev. Lett. **112**, 023602 (2014).
[22] Q. Liao and U. Thumm, Phys. Rev. A **89**, 033849 (2014).
[23] C. A. Rios Rubiano, M. S. Gravielle, D. M. Mitnik, and V. M. Silkin, Phys. Rev. A **85**, 043422 (2012).
[24] A. K. Kazansky and P. M. Echenique, Phys. Rev. Lett. **102**, 177401 (2009).
[25] J. C. Baggesen and L. B. Madsen, Phys. Rev. A **78**, 032903 (2008).
[26] See Supplemental Material at http://link.aps.org/supplemental/10.1103/PhysRevLett.125.043201 for the

derivation from a semiclassical model, which includes Refs. [27–29].

[27] J. Li, E. Saydanzad, and U. Thumm, Phys. Rev. Lett. **120,** 223903 (2018).

[28] J. Li and U. Thumm, Phys. Rev. A **101,** 013411 (2020).

[29] E. V. Chulkov, V. M. Silkin, and P. M. Echenique, Surf. Sci. **437,** 330 (1999).

[30] M. Lucchini, L. Castiglioni, L. Kasmi, P. Kliuiev, A. Ludwig, M. Greif, J. Osterwalder, M. Hengsberger, L. Gallmann, and U. Keller, Phys. Rev. Lett. **115,** 137401 (2015).

[31] M. J. Ambrosio and U. Thumm, Phys. Rev. A **94,** 063424 (2016).

[32] M. J. Ambrosio and U. Thumm, Phys. Rev. A **96,** 051403 (R) (2017).

[33] A. Zangwill, *Physics at Surfaces* (Cambridge University Press, Cambridge, England, 1988).

[34] S. Hüfner, *Photoelectron Spectroscopy: Principles and Applications*, 3rd ed. (Springer, Berlin, 2003).

[35] C.-H. Zhang and U. Thumm, Phys. Rev. A **84,** 063403 (2011).

On the distinction of electron dispersion in time-resolved photoemission spectroscopy

Qing Liao,[1,*] Wei Cao,[2] Qingbin Zhang,[2] Kai Liu,[1] Feng Wang,[1] Peixiang Lu,[1,2,3†], and Uwe Thumm[4,‡]

[1] Hubei Key Laboratory of Optical Information and Pattern Recognition,
Wuhan Institute of Technology, Wuhan 430205, China
[2] Wuhan National Laboratory for Optoelectronics and School of Physics,
Huazhong University of Science and Technology, Wuhan 430074, China
[3] CAS Center for Excellence in Ultra-intense Laser Science, Shanghai 201800, China
[4] Department of Physics, Kansas State University, Manhattan, KS 66506, USA

(Dated: May 29, 2020)

SEMI-CLASSICAL MODEL FOR PHOTOEMISSION FROM REAL SOLIDS

The transition amplitude for photoemission from an initial state $\psi_i(z,t) = \psi_i(z)e^{-i\varepsilon_i t}$ by a high-harmonic (HH) component of the APT with photon energy $(2q+1)\omega_{IR}$ is given by

$$T_{k_f,2q+1}(\tau) \propto \int dt \langle \psi_{k_f,2q+1}(z,t)| A_{X,2q+1}(t)\frac{\partial}{\partial z}|\psi_i(z,t)\rangle. \quad (1)$$

We semi-classically model the final photoelectron state as a heuristically generalized damped Volkov wavefunction [1–4],

$$\psi_{k_f,2q+1}(z,t) = D(z,\lambda)e^{-i\xi_{2q+1}(z)+i\phi_{MV}(z,k_f,t)}, \quad (2)$$

with the spatial phase

$$\xi_{2q+1}(z) = \int_z^\infty dz'k(z',t'), \quad (3)$$

and the modified temporal Volkov phase

$$\phi_{MV}(z,k_f,t) = \varepsilon_{2q+1}(t_{s,2q+1}-t) + \phi_V(k_f,t_{s,2q+1}), \quad (4)$$

given in terms of the ordinary Volkov phase $\phi_V(k_f,t) = \int_t^\infty dt'[k_f + A_L(t'-\tau)]^2/2$. The semi-classical representation of $\psi_{k_f}(z,t)$ consists in calculating the photoelectron phase along a classical trajectory $z'(t')$. $\varepsilon_{2q+1} = \varepsilon_i + (2q+1)\omega_{IR}$ is the energy of photoelectron *inside* the solid. We assume that the IR laser field is fully screened at the exit surface located at the image plane position z_{im} and the photoelectron reaches z_{im} at time $t_{s,2q+1}$. The damping function $D(z,\lambda) = e^{-|z-z_{im}|/(2\lambda)}$, where λ is the energy-dependent mean-free path, describes the decrease of photoelectron amplitude due to elastic and inelastic scattering in the solid. The transition amplitude

---
*liaoqing@wit.edu.cn
†lupeixiang@mail.hust.edu.cn
‡thumm@phys.ksu.edu

(1) can now be written as

$$T_{k_f,2q+1}(\tau) \propto A_{X0,2q+1}e^{-i\varphi_{2q+1}}\int dt f_X(t)e^{-i(2q+1)\omega_{IR}t}$$
$$\times \int dz \times D(z,\lambda)e^{i[\xi_{2q+1}(z)-\phi_{MV}(z,k_f,t)]}\frac{\partial}{\partial z}\psi_i(z,t). \quad (5)$$

We consider sufficiently high photoelectron kinetic energies (i.e., sufficiently large XUV-photon energies) such that $k_f >> |A_{L0}(t)|$ and the Wigner and (IR-pulse-induced) continuum-continuum-transition time delays can be neglected compared with the transport time [5]. For a slowly varying envelope $A_{L0}(t)$, the vacuum part of the Volkov phase can then be approximated as $\phi_V(k_f,t) \approx -k_f^2/2t-x(t)sin[\omega_{IR}(t-\tau)]$, where $x(t) = k_f A_{L0}(t-\tau)/\omega_{IR}$. Disregarding the slow variation of x with time, we can apply the Jacobi-Anger expansion in Bessel functions $J_n(x)$ at $t = t_{s,2q+1}$,

$$e^{ixsin[\omega_{IR}(t-\tau)]} = \sum_{n=-\infty}^{\infty}J_n(x)e^{in[\omega_{IR}(t-\tau)]}, \quad (6)$$

to approximate (5) as

$$T_{k_f,2q+1}(\tau) \propto A_{X0,2q+1}e^{-i\varphi_{2q+1}}\int dt f_X(t)$$
$$\times e^{i(k_f^2/2-\varepsilon_{2q+1})t_{s,2q+1}}\sum_{n=-\infty}^{\infty}e^{in\omega_{IR}(t_{s,2q+1}-\tau)}$$
$$\times \int dz J_n[x(t_{s,2q+1})]D(z,\lambda)e^{i\xi_{2q+1}(z)}\frac{\partial}{\partial z}\psi_i(z)$$
$$=: \sum_{n=-\infty}^{\infty}T_{k_f,2q+1,n}(\tau). \quad (7)$$

Since for weak laser fields $x << 1$, only the term with $n = 0$, corresponding to single-photon emission by the spectral HH component $A_{X,2q+1}(t)$ with photon energy $(2q+1)\omega_{IR}$, and first-order SB terms with $n = \pm 1$ contribute to the photoelectron yield. Interference of the two SB terms and use of the identity $J_{-1}(x) = e^{i\pi}J_1(x)$

results in the SB-$2q$ amplitude

$$T_{k_f,2q}(\tau) = T_{k_f,2q-1,n=-1}(\tau) + T_{k_f,2q+1,n=1}(\tau)$$
$$\propto \int dt f_X(t) \int dz D(z,\lambda) \frac{\partial}{\partial z} \psi_i(z)$$
$$\times \{A_{X0,2q-1} J_1[x(t_{s,2q-1})] e^{i[-\varphi_{2q-1}+\xi_{2q-1}(z)+\omega_{IR}\tau+\pi]}$$
$$\times e^{i(k_f^2/2-\varepsilon_{2q-1}-\omega_{IR})t_{s,2q-1}}$$
$$+ A_{X0,2q+1} J_1[x(t_{s,2q+1})] e^{i[-\varphi_{2q+1}+\xi_{2q+1}(z)-\omega_{IR}\tau]}$$
$$\times e^{i(k_f^2/2-\varepsilon_{2q+1}+\omega_{IR})t_{s,2q+1}}\}. \tag{8}$$

Evaluated at the central SB-$2q$ energy $k_f^2/2 = \varepsilon_i + 2q\omega_{IR}$ and $\varepsilon_{2q\pm1} = \varepsilon_i + (2q\pm1)\omega_{IR}$, the total phase difference between the contributions for IR-photon emission ($n=1$) and the absorption ($n=-1$) in Eq. (8) is

$$\Delta\Phi_{2q} = \Delta\xi_{2q}(z) - \Delta\varphi_{2q} - \pi - 2\omega_{IR}\tau, \tag{9}$$

with the HH phase difference $\Delta\varphi_{2q} = \varphi_{2q+1} - \varphi_{2q-1}$. Writing the spatial phase accumulation as

$$\xi_{2q\pm1}(z) = k_{2q\pm1}(z_{im} - z) + \int_{z_{im}}^{\infty} dz' k_f, \tag{10}$$

where the momentum $k_{2q\pm1}$ *inside* the solid corresponds to the energy $\varepsilon_{2q\pm1}$, and assuming the initial states are localized at z, the spatial propagation-phase difference between the interfering SB channels becomes

$$\Delta\xi_{2q}(z) = \xi_{2q+1}(z) - \xi_{2q-1}(z)$$
$$= (k_{2q+1} - k_{2q-1})(z_{im} - z). \tag{11}$$

SIMULATION OF RABITT PHOTOEMISSION SPECTRA FROM CORE-LEVEL STATES

We model Mg-$2p$ core-level (CL) states by adding the Yukawa potential

$$U_Y(z) = -e^{-|z-z_j|/\zeta}/\sqrt{(z-z_j)^2 + a_0^2}, \tag{12}$$

where z_j is the position of the j'th atom, to the Chulkov potential $U_C(z)$ [6] with parameters corresponding to the Mg(0001) surface [7]. By adjusting the screening length $\zeta = 1.2$ and the soft-core parameter $a_0 = 0.243$, the combined potentials yield highly localized Mg-$2p$ CL states (see Fig. 1 of this supplement) with a narrow bandwidth of 0.4 eV and binding energies near -53 eV, both very close to those found experimentally [8].

The sideband photoemission spectra of Mg-$2p$ photoelectrons along the normal direction of the Mg(0001) surface are calculated according to Eq. (8). We use the same attosecond pulse train and IR laser parameters as in the main text and assume the IR laser fully screened at the image plane z_{im}=3.46 a.u. We assume a parabolic energy-momentum relation for photoelectrons traveling
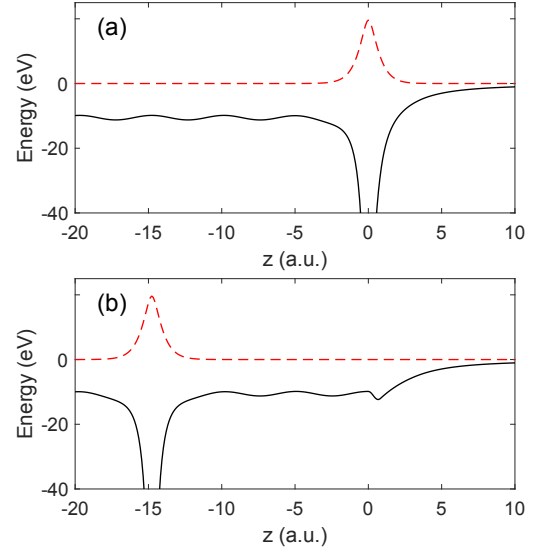

FIG. 1: (color online). Effective potentials $U_Y(z) + U_C(z)$ (solid black line) are used to model the wavefunctions of Mg-$2p$ core-level states (dashed red line). Wavefunctions of core-level states at (a) the surface layer and (b) the fourth layer.

inside the solid. We keep the effective mass for photoelectrons excited by HH order 51 equal to one ($m_{e,51} \equiv 1$). We change the effective mass $m_{e,49}$ for photoelectrons excited by HH order 49 to demonstrate the strong dependence of the energy-momentum dispersion on the measured photoemission time delays. The lattice constant is $a_s = 4.923$ a.u.. The mean-free path is taken as $\lambda = 10$ a.u., for the considered energies [9]. Figures 2(a)-2(c) of this supplement show the calculated spectra of sideband-50 photoelectrons from core-level states located at the topmost 15 lattice sites for $m_{e,49} = 0.8$, 1, and 1.4 a.u.. Due to the finite mean-free path, contributions from core-level states in deeper lattice sites can be neglected. The corresponding total yield oscillations with the XUV-IR delay are shown in Fig. 3 of this supplement.

[1] Q. Liao and U. Thumm, Phys. Rev. Lett. **112**, 023602 (2014).
[2] Q. Liao and U. Thumm, Phys. Rev. A **89**, 033849 (2014).
[3] J. Li, E. Saydanzad, and U. Thumm, Phys. Rev. Lett. **120**, 223903 (2018).
[4] J. Li and U. Thumm, Phys. Rev. A **101**, 013411 (2020).
[5] K. Klünder *et al.*, Phys. Rev. Lett. **106**, 143002 (2011).
[6] E. V. Chulkov, V.M. Silkin, and P. M. Echenique, Surf. Sci. **437**, 330 (1999).
[7] A. K. Kazansky and P. M. Echenique, Phys. Rev. Lett. **102**, 177401 (2009).
[8] S. Neppl, R. Ernstorfer, E.M. Bothschafter, A. L. Cavalieri, D. Menzel, J. V. Barth, F. Krausz, R. Kienberger, and P. Feulner, Phys. Rev. Lett. **109**, 087401 (2012).
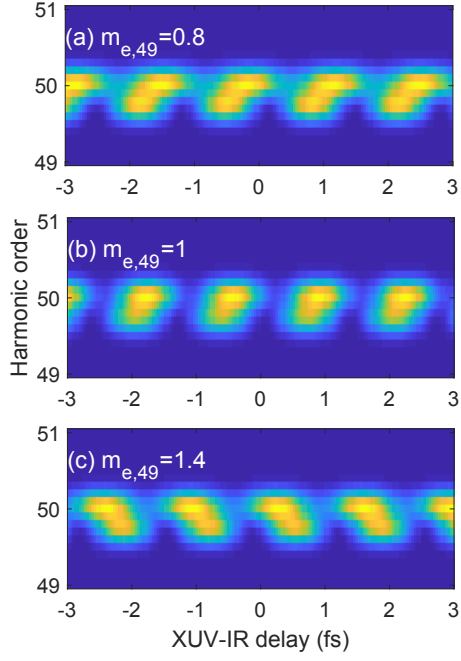[9] A. Zangwill, *Physics at Surfaces* (Cambridge University

FIG. 2: (color online). Spectra of sideband-50 photoelectrons from Mg-2p core-level states on a linear color scale versus the XUV-APT-IR pulse delay τ for different effective mass: $m_{e,49} = 0.8$ (a), 1 (b), and 1.4 (c), and $m_{e,51} \equiv 1$ a.u..
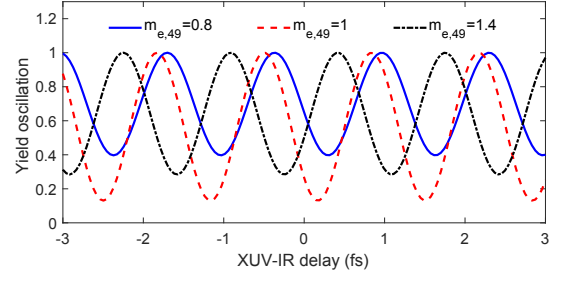

FIG. 3: (color online). Normalized yield oscillations of sideband-50 photoelectrons with the XUV-APT-IR pulse delay τ for different effective mass.

Press, Cambrigdge, England, 1988).